ISBN 82–553–0887–3
Mechanics and
Applied Mathematics

No. 1

February 1994

Numerical simulations of tsunami waves: Preliminary results of the Storegga, the Gorringe bank and the Thera case studies

by

B. Gjevik, G. Pedersen, E. Dybesland and C. B. Harbitz

PREPRINT SERIES – Matematisk institutt, Universitetet i Oslo

Numerical Simulations of Tsunami Waves: Preliminary results of The Storegga, The Gorringe Bank and The Thera Case Studies

by

B. Gjevik, G. Pedersen, E. Dybesland, and C. B. Harbitz

Department of Mathematics, University of Oslo,
P.O.Box 1053 Blindern, Oslo, Norway.

January 31, 1994

Abstract

This report summarizes preliminary results of model development and simulations as part of the activity under the EU research project; Genesis and Impact of of Tsunami waves on the European Coasts (GITEC). Three test cases have been examined; the tsunami from the Storegga slide in the Norwegian Sea 7000 BC, the earthquake generated tsunami from Gorringe Bank west of Portugal in 1969, and the possible tsunami from an exploding volcano on the island of Thera in the Aegean Sea 1640 BC.

A linear hydrostatic shallow water model is used for most of the simulations, but the importance of nonlinearity and dispersion is studied by a model based on the Boussinesq equations. The sensitivity of the solution to changes in the location and the strength of the source is discussed in particular for the 1969 event.

The results of the simulations are compared with available observations and geological evidence of tsunami runup. For the 1969 event, with source near Gorringe Bank, the agreement between between modelled and observed wave amplitude and period along the coast of Portugal is good.

1 Introduction

The common European research project "Genesis and Impact of Tsunami waves on the European Coasts" (GITEC) consists of 9 different research groups; two from Italy (Bologna and Genoa), one from England (Coventry), one from France (Paris), one from Portugal (Lisboa), two from Athens, Greece and two from Norway (Bergen, Oslo). The Oslo group

has engaged in model development and test case simulations. This report summarizes work done by the Oslo group in the period from January to December 1993.

The focus of the report is on results of model simulation of tsunami wave generation in three cases; the Storegga slide on the shelf west of Norway 7000 years BC, the 1969 earthquake near the Gorringe Bank southwest of Portugal, and a collapsing volcano on Thera in the Greek Archipelago 1640 BC.

The simulations are primarily done with a linear hydrostatic shallow water model, but in order to check the validity of the approximation we have for comparison also performed simulations with the Boussinesq equations. This enables a discussion of the effects of wave dispersion, non-linearity and discretization errors.

Besides the work with the test cases we have undertaken a substantial model upgrading in order to develop flexible and efficient routines for running simulation experiments and making comparisons with observations. The pay-off of this work will show in the near future when the work is focused on a better tuning of the model to observational data.

2 Basic Model Equations and Numerical Method.

In this study we have employed the shallow water equations of various orders. For long waves the relative importance of nonlinearity and dispersion can be measured by the dimensionless parameters α =(amplitude/depth) and ϵ =(depth/wavelength)^2 respectively. The simplest long wave theory yields the linearized shallow water equations that are valid to the leading order in α and ϵ only. In this approximation the pressure is hydrostatic and the waves display no dispersion. A common extension is the Boussinesq type equations that appear in the literature in a large number of varieties. The Boussinesq equations used herein inherit relative errors of order $\epsilon^2, \epsilon\alpha$ which mean that the formulation is strongly nonlinear but only weakly dispersive. When the $O(\epsilon)$ terms are deleted the Boussinesq equations reduce to the well known Airy equations that are frequently used for describing hydraulic jumps etc.

Since the effects of dispersion and nonlinearity are accumulated over time the values of α and ϵ alone do not determine the applicability of the different shallow water equations. However, as a rule of thumb the hydrostatic approximation is good for values of ϵ up to 0.01 , say, whereas most shallow water equation tolerate quite steep bottom slopes for practical use.

2.1 The linear hydrostatic shallow water equations

The governing equations are formulated in a Cartesian coordinate system on a stereographic map projection. This transformation has the advantage that the numerical computation can be performed on a Cartesian grid where each grid box covers an area of approximately the same extent. Details on the stereographic map projection is given in section 3. The linearized equation of motion transformed to a Cartesian coordinate system with axis

(x, y) in the horizontal plane read;

$$\frac{\partial u}{\partial t} = -mg\frac{\partial \eta}{\partial x} + \frac{\tau_x}{\rho h} \tag{1}$$

$$\frac{\partial v}{\partial t} = -mg\frac{\partial \eta}{\partial y} + \frac{\tau_y}{\rho h} \tag{2}$$

where (u, v) are the corresponding components of the mean current velocity, η is the vertical displacement of the sea surface from its undisturbed position, m is the map factor defined in section (3), and g is the acceleration of gravity. (τ_x, τ_y) are the components of the bottom stress introduced by the slide motion, and ρ is the density of sea water.

The continuity equation reads

$$\frac{\partial \eta}{\partial t} = -m^2\left[\frac{\partial}{\partial x}(\frac{uh}{m}) + \frac{\partial}{\partial y}(\frac{vh}{m})\right] - \frac{\partial h}{\partial t} \tag{3}$$

where the term $\frac{\partial h}{\partial t}$ represents the depth changes due to the slide or the earthquake motion.

The bottom stress vector is parameterized by

$$\tau_x = -\rho c_D \Delta w \Delta u \tag{4}$$

$$\tau_y = -\rho c_D \Delta w \Delta v \tag{5}$$

where Δu and Δv denote the components of the velocity difference between the slide body and the fluid above and

$$\Delta w = \sqrt{(\Delta u^2 + \Delta v^2)} \tag{6}$$

c_D is the drag coefficient.

The equations of motion (1-3) have been discretized on a space staggered C-grid ([10]) with an explicit centered differences scheme [8]. The scheme has been widely used for depth integrated ocean models and the stability criteria for the scheme is

$$\Delta t \leq \frac{\Delta s}{\sqrt{2g(mh)_{max}}} \tag{7}$$

where Δs is half the grid size i.e. the distance between neighbor points where elevation and current are evaluated and h_{max} the maximum water depth. Further details are found in the papers referred above.

2.2 The Bousinessq equations

The higher order long wave equations will be applied primarily for analyzing local effects for example near the tsunami source. The map factor, m, may consequently be set to 1. We will express the Boussinesq equations in terms of the surface elevation, η, as described above and the depth averaged velocity potential:

$$\overline{\phi} = (h + \eta)^{-1} \int_{-h}^{\eta} \phi dz \tag{8}$$

where ϕ relates to the velocity according to $\nabla\phi = \vec{v}$. The continuity equation reads

$$\frac{\partial \eta}{\partial t} + \frac{\partial h}{\partial t} = -\nabla \cdot \vec{Q} \tag{9}$$

where the integrated volume flux density, $\vec{Q}$, is given according to

$$\vec{Q} = h\nabla\overline{\phi} + \eta\nabla\overline{\phi} + h(\frac{1}{6}\frac{\partial \eta}{\partial t} - \frac{1}{3}\frac{\partial h}{\partial t} - \frac{1}{3}\nabla h \cdot \nabla\overline{\phi})\nabla h \tag{10}$$

The second term on the right hand side is nonlinear whereas the quantities within the parentheses represent contributions of higher order in ϵ. The equations of motion (1-2) are replaced by the single Bernoulli equation:

$$\frac{\partial \overline{\phi}}{\partial t} + g\eta + \frac{1}{2}(\nabla\overline{\phi})^2 - \{\frac{1}{2}h\frac{\partial^2 h}{\partial t^2} + \frac{1}{2}h\nabla\cdot(h\nabla\frac{\partial\overline{\phi}}{\partial t}) - \frac{1}{6}h^2\nabla^2\frac{\partial\overline{\phi}}{\partial t}\} = 0 \tag{11}$$

where the third term is nonlinear and the embraced term is of higher order in ϵ (dispersion term). Concerning the derivation of the above equations we refer to [18] and [15].

As compared to the set 1-3 the complexity of the above equations is increased by an order of magnitude. Most important are the principally new terms that are nonlinear or involves higher order differentiation. Consequently numerical solution of the Boussinesq equations is a much heavier task than the solution of the linear hydrostatic equations. The procedure applied below is described in detail in [14], [15] and [16].

The introduction of a velocity potential simplifies the Boussinesq equations substantially, especially in relation to finite element techniques. However, the velocity potential exists for irrotational motion only. Hence, when the bottom stress or the Coriolis force is taken into account the set (9) through (11) must be replaced by a description based on velocities. A numerical solution procedure for such equations is given in [14].

3 The stereographic map projection

The stereographic map projection is normally used for high latitudes with the pole of the projection at the geographical pole [6]. When working on lower latitudes the pole of projection can be shifted to the center of domain of interest and the equations of motion transformed to a Cartesian coordinate system with the (x,y)-axis in a horizontal plane tangential to the earth at the pole of the projection (fig. 1, 2).

Let (B_o,L_o) and (B,L) denote respectively the latitude, longitude of the pole of the projection, P_o, and a point P near the pole. The origo of the Cartesian coordinate system is chosen at P_o with the x and y axis pointing respectively in eastward and northward direction. The point P on the earth is projected to P' on the xy-plane with coordinates

$$x = r\cos(\theta - \frac{\pi}{2}) \tag{12}$$

$$y = r\sin(\theta - \frac{\pi}{2}) \tag{13}$$

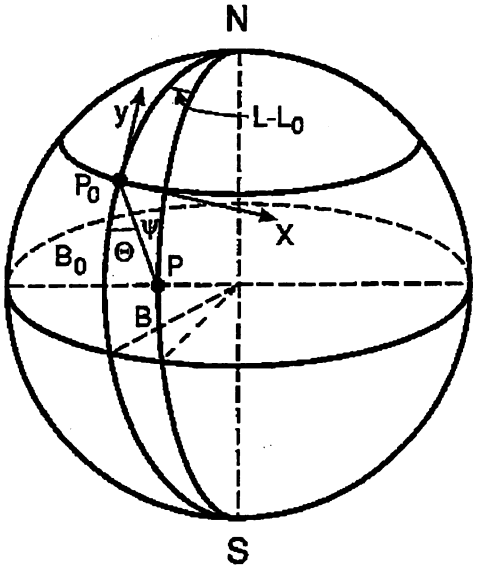

Figure 1: Definition of spherical angles related to the pole of the stereographic projection

where

$$r = 2R\tan(\frac{\psi}{2}) \tag{14}$$

R is the radius of the Earth, θ is the azimuthal direction of the great circle arc between P_o and P, with the understanding that $\theta = 0°$ when P is due south of P_o and $\theta = 180°$ when P is due north of P_o. ψ is the length of the great circle between P_o and P measured in radians. The great circle arc P_oP is mapped as a straight line P_oP' on the xy-plane.

From formulas in spherical geometry we have:

$$\cos\psi = \sin B_o \sin B + \cos B_o \cos B \cos(L - L_o) \tag{15}$$

and

$$\cos\theta = \frac{\sin B_o \cos\psi - \sin B}{\cos B_o \sin\psi} \tag{16}$$

The formulas above can be used for finding the Cartesian coordinates (x,y) when the geographical coordinates (B,L) are given. For the inverse transformation from (x,y) to (B,L) another set of formulas obtained by rewriting (15 - 16) are useful

$$\sin B = \sin B_o \cos\psi - \cos B_o \sin\psi \cos\theta \tag{17}$$

and

$$\cos(L - L_o) = \frac{\cos\psi - \sin B_o \sin B}{\cos B_o \cos B} \tag{18}$$

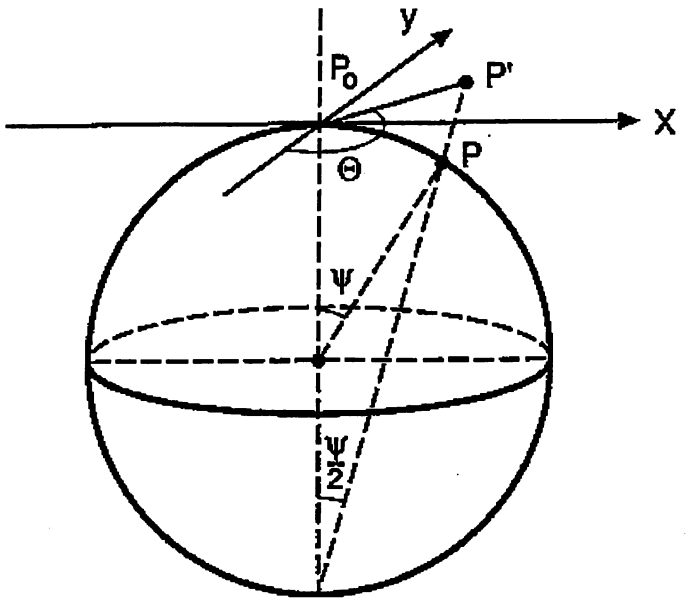

Figure 2: Definition of axis and angles in projection plane

The map factor (m) relates the length of a line element on the sphere to its image on the plane;

$$m = \frac{2}{1 + \cos\psi} \tag{19}$$

For wave propagation over relatively short distances near the pole the map factor is ≈ 1. For the simulations reported below we have therefore applied $m = 1$.

4 Implementation of the tsunami source

Water wave generation by slides, earthquake faulting and collapsing volcanos depends primarily on the large scale displacement of water or the vertical motion of the sea bed. For slides the shear stress along the slide body may in some cases be important. Since detailed data for the shape and time evolution of the sources generally are not available we have to rely on idealized model descriptions. However, in spite of the inherent simplicity of these models we still believe that the source models possess sufficient flexibility to yield an adequate representation of most real events.

We utilize a limited number of shape and time evolution functions to model the changes in the sea bed due to earthquake faulting, caldera formation and submarine slides . These functions are summarized in appendix A. For each shape function the source can be tuned to match real events by means of the parameters:

Table 1: Source parameters

Δh	Amplitude of bottom displacement.
a, b	Horizontal length scales of slide, fault or caldera
θ	Angle for orientation of source or direction of slide advance.
x_0, y_0	Initial position for center of source.
T	Time scale for faulting or slide event.
L	Total travel distance for slide.

The angle θ is measured relative to the x-axis and a and b denotes respectively the extensions along and normal to the direction indicated by θ. Denoting the shape function by S we may now express the changes in bottom topography due to a fault or caldera formation by;

$$h = h_0 - \Delta h G(t) S\left(\frac{x'}{a}, \frac{y'}{b}\right) \tag{20}$$

where h_o denotes the undisturbed depth and $G(t)$ is a time evolution factor conveniently chosen as

$$G(t) = \begin{cases} \frac{1}{2}(1 - \cos(\frac{\pi t}{T})) & 0 < t < T \\ 1 & t > T \end{cases}$$

The coordinate axis x', y' are defined relative to the orientation of the source by;

$$x' = (x - x_o)\cos\theta + (y - y_o)\sin\theta \qquad y' = -(x - x_o)\sin\theta + (y - y_o)\cos\theta \tag{21}$$

The changes in depth due to a moving slide body is correspondingly represented by:

$$h = h_0 - \Delta h S\left(\frac{x' - LG(t)}{a}, \frac{y'}{b}\right) \tag{22}$$

where $LG(t)$ is measure for the distance travel by the slide.

For earthquake faulting and collapsing volcanos we must generally expect small values of T. Provided $T \ll (gh_0)^{-\frac{1}{2}} \max(a, b)$ we may regard the bottom deformation as instantaneous which implies that the disturbance at $t = 0$ may be described as a sea surface displacement of the form $\Delta h S(x', y')$.

5 Analytical solution for waves generated by motion of the sea bed

For uniform depth h_o = constant, analytical solutions of the linearized equation of motion (1 - 3) can be obtained for prescribed vertical displacement of the sea bed, [9]. We consider a symmetrical impulsive displacement of the sea bed in form of a Gaussian bell (24). The

center of the displacement area is at $r = 0$ with typical radius of extent $a = b$ and amplitude of the uplift Δh. The corresponding surface displacement is given by;

$$\eta(r,t) = \frac{\Delta h a^2}{2} \int_0^\infty \exp(-\frac{a^2k^2}{4})\, J_0(kr)\, k \cos kct\, dk \tag{23}$$

Here $c = \sqrt{gh_o}$ denotes the wave speed, the integration parameter k is a spatial wave number and $J_0(kr)$ denotes the zero order Bessel function. The integral solution can be used for checking the numerical model and also to determine the relation between the source parameters and the amplitude and the period of the tsunami wave. By introducing dimensionless variables where time, distance and wave number are scaled respectively by $\frac{a}{c}$, a and $\frac{1}{a}$ the similarity properties of the function $\eta(r,t)$ become obvious.

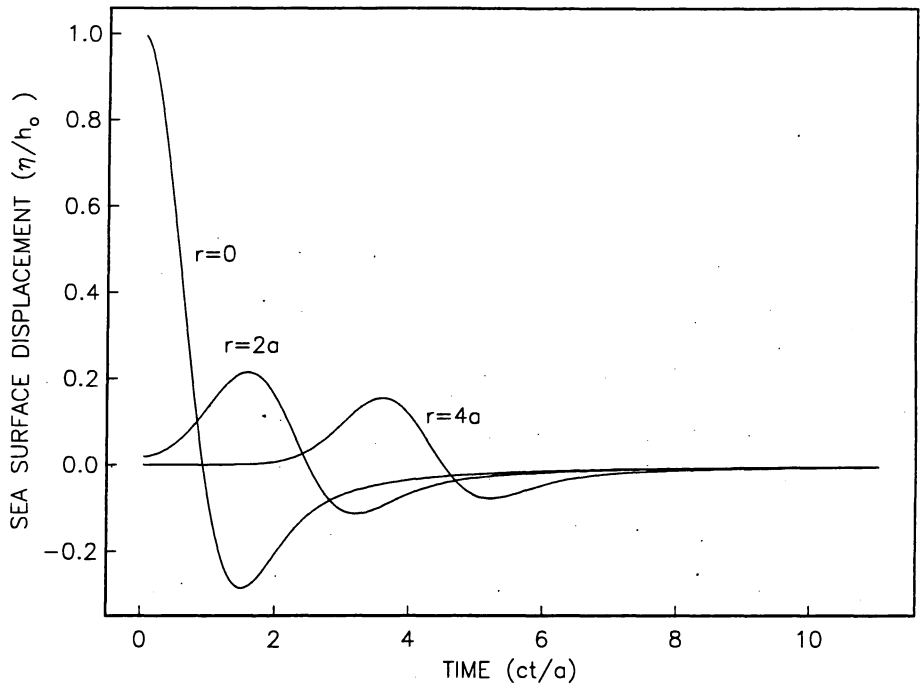

Figure 3: Sea surface displacement (scaled) as function of time for three positions along the radial axis $r = 0$, $2a$, and $4a$.

The signal resembles a single wave with a first large peak followed by a smaller displacement of opposite sign (fig 3). As a measure of the period of the wave , t_p, twice the time span between the maximum and the minimum displacement can be used. For r larger than a we find $t_p \approx \frac{3.3a}{c}$ which shows that the period of the wave increases linearly with the radius of the disturbance and decreases with increasing wave speed.

6 Simulations of the coastal response of the Storegga tsunami.

The tsunami generation and propagation due to the Storegga slide has previously been simulated by [7] with a 12.5 km grid resolution covering the Nordic Seas. The model predicted high waves along the western coast of Norway about 100 km east of the shelf break where the slide started. The model did not resolve the complex geometry of these coastal areas with fjords and islands. For this reason it did not render any information on local amplification effects in the coastal zone.

Detailed information on the run-up pattern in the coastal zone is useful for the GITEC group at the University of Bergen when choosing new sites for coring after possible tsunami deposits. In order to study the tsunami propagation into the coastal area we have developed a high resolution coastal model.

A depth matrix with 500 m grid resolution (fig. 4) covering a rectangular section, 270 km x 290 km, of the coast from Ålesund on Møre to Vikna in Nord-Trøndelag was already available to us from a project on modelling tidal and wind driven currents [5]. Along the western and northern boundary of the coastal model domain we used interpolated surface displacement from the large scale Storegga model as input data.

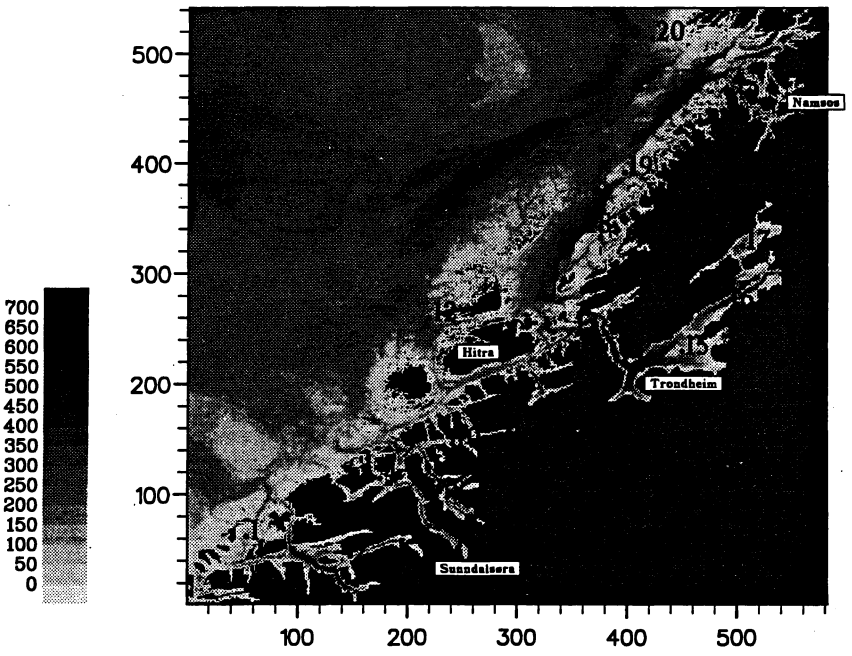

Figure 4: The Storegga case: Depth matrix with location of stations with modelled time series for sea surface displacement. Grid coordinates on axis with grid resolution 500 m.

The simulations of tsunami propagation in the coastal zone show interesting dynamics with wave amplification due to bottom topography and trapping of wave energy in fjord basins (fig.4 and fig. 6a,b). Predicted wave amplitudes in the area southwest of Ålesund are

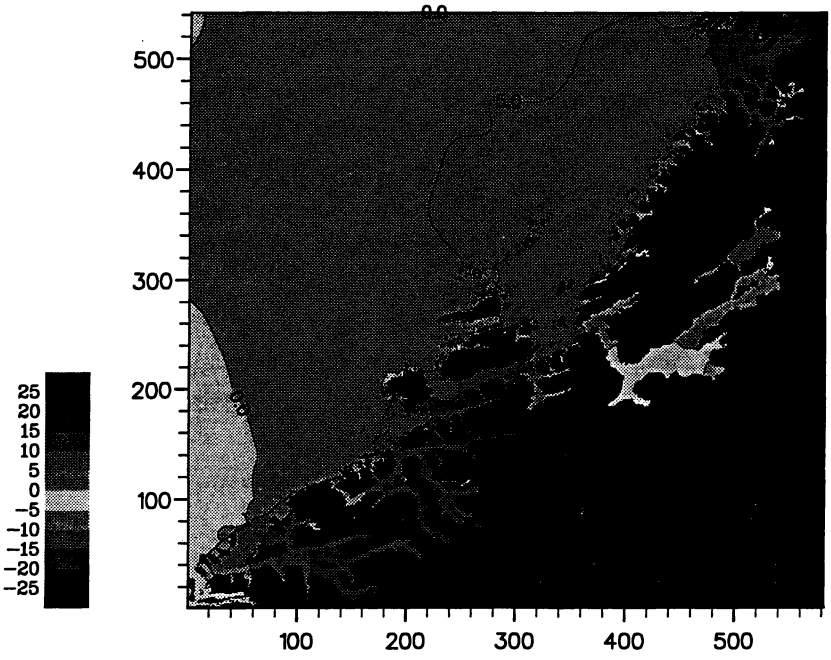

Figure 5: The Storegga case: Contour plot of sea surface displacement (m) at time 3 5 hours after release of slide.

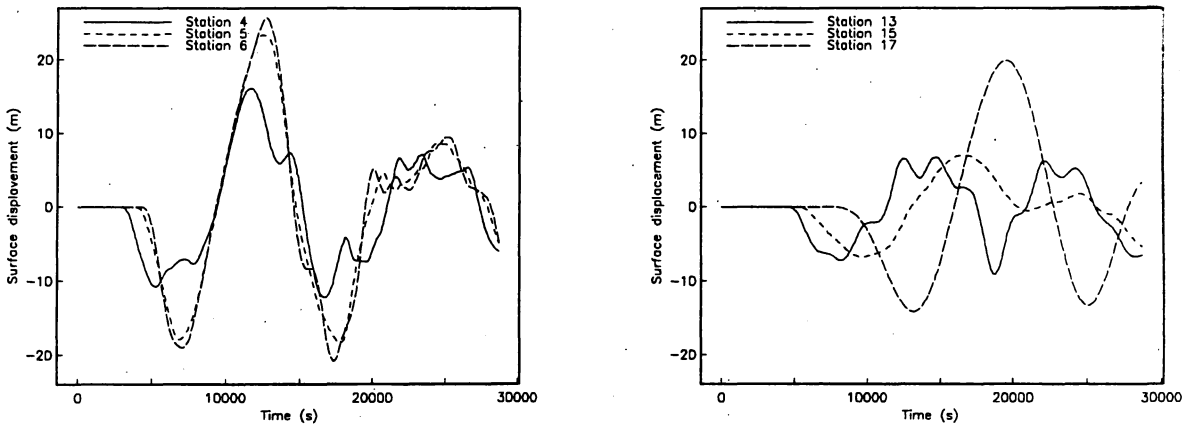

a) b)

Figure 6: The Storegga case: Time series for sea surface displacement: Sunndalsfjorden station 4, 5 and 6 (a). Trondheimsfjorden station 13, 15, 17 (b).

consistent with evidence of run-up heights deduced from analyzing recent coring samples from Gurkøy ([3]). The model also predicts high amplitudes along the coast from Hustavika on Møre to Fosna in Trøndelag. Results of the analysis of core samples taken in the summer 1993 in Trøndelag ([3]), show possible tsunami deposits on two locations in Bjugn (west of station 13,fig.5a . The tsunami runup height is probably between 5 and 15 m which is considerable less than predicted by the model. In the inner Trondheimsfjord no tsunami deposits have been yet identified, but coring in basins responding to wave height less then 15 m remains to be done.

In view of the geological evidence of wave amplitudes, the Storegga model should be re-run in order to investigate the effect of a reduced slide volume. Recent geological surveys of the Storegga slide area also indicate that the slide may have occurred as several separate events. A sensitivity study of the model results to grid refinement and different nesting boundary conditions along the open ocean boundaries of the subdomain model should also be performed.

7 The Gorringe Bank case study

7.1 Observation of tsunamis

The Azores-Gibraltar fracture zone with the huge bathymetric reliefs in the area southwest of Cabo São Vicente in southern Portugal is believed to have been the source of large historic tsunami events destroying the city of Lisbon at least twice in January 1531 and November 1755 [2]. The 28 February 1969 earthquake with epicenter south of the Gorringe Bank generated a small tsunami which was recorded on tide gauges along the coasts of Spain and Portugal. The tsunami signal has been separated from the tide record by a maximum entropy spectral analysis [2]. The amplitude range ie. the difference between the maximum and the minimum wave displacement at Lagos and Cascais was estimated to 0.84 and 0.93 m respectively. The corresponding tsunami periods were 14.4 and 19.2 minutes and travel time 35.5 and 37.0 minutes. According to historic records the amplitude of the 1755 tsunami, which often is said to have originated in the same area as the 1969 event, was 6 m at Lisbon and 30 m at Sagres near Cabo São Vicente.

In view of the observed evidence we have attempted to model tsunami generation and propagation from a source located in the Gorringe Bank area.

7.2 The depth matrix

A depth matrix with 3 minutes $\times$ 3 minutes longitude latitude grid resolution has been compiled for the area west of Portugal and made available to us by the courtesy of the Lisbon group. The matrix is obviously hampered with minor errors which are most visible along the coastlines. We have applied the stereographic map projection (see section 3) and by interpolation in the longitude-latitude grid generated a depth matrix on a Cartesian grid with 5 km $\times$ 5 km resolution covering an area of 2000 km $\times$ 2000 km. The pole of the projection is chosen at 35° N and 16° W at the center of the domain (fig. 7). The details of

the bathymetric features near the Gorringe Bank as depicted by the corrected interpolated depth matrix is shown in section 7.5, fig. (11a).

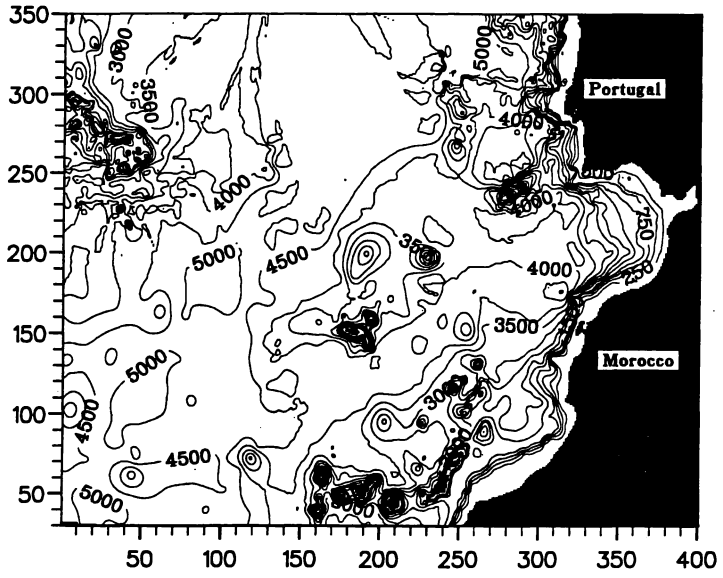

Figure 7: Model domain southwest of Portugal. Stereographic map projection with pole at 35° N, 16° W. Grid resolution: 5 km. Grid coordinates shown on axis.

7.3 Models of tsunami source

The source model which we have implemented rests on ideas that came up during the GITEC meeting in Wiesbaden and later through discussions with professor A. Ribeiro, University of Lisboa. The European plate override the African plate with a reverse fault parallel to the axis of the Gorringe ridge, the 1969 event being clearly a thrust fault with epicenter determined to be south of the Gorringe Bank ([4]). The exact location of the epicenter is however questionable and the ray tracing technique used by [2] indicates that the tsunami source was located on the northern side of the Gorringe ridge.

Associated with an earthquake event near Gorringe Bank one should expect an upward motion of the seabed over an area on the northern side of the fault with small downward motion over a smaller area on the southern side of the fault. The asymmetry in upward and downward motion depending on the properties of the crustal materials and the orientation of the fault etc. Geological evidence for a lifting of the Gorringe Bank with an average velocity of 0.4 m per 100 years for the last 20.000 years has been given by [17]. Assuming a return period of 250 years for a large ruptures on the fault, this will imply an upward displacement of the seabed during a major event of the order of 1 m.

According to these considerations the the seabed motion during the 1969 tsunami event is modelled by lifting the seabed in a rectangular area ($a \times b$) where b is measured parallel

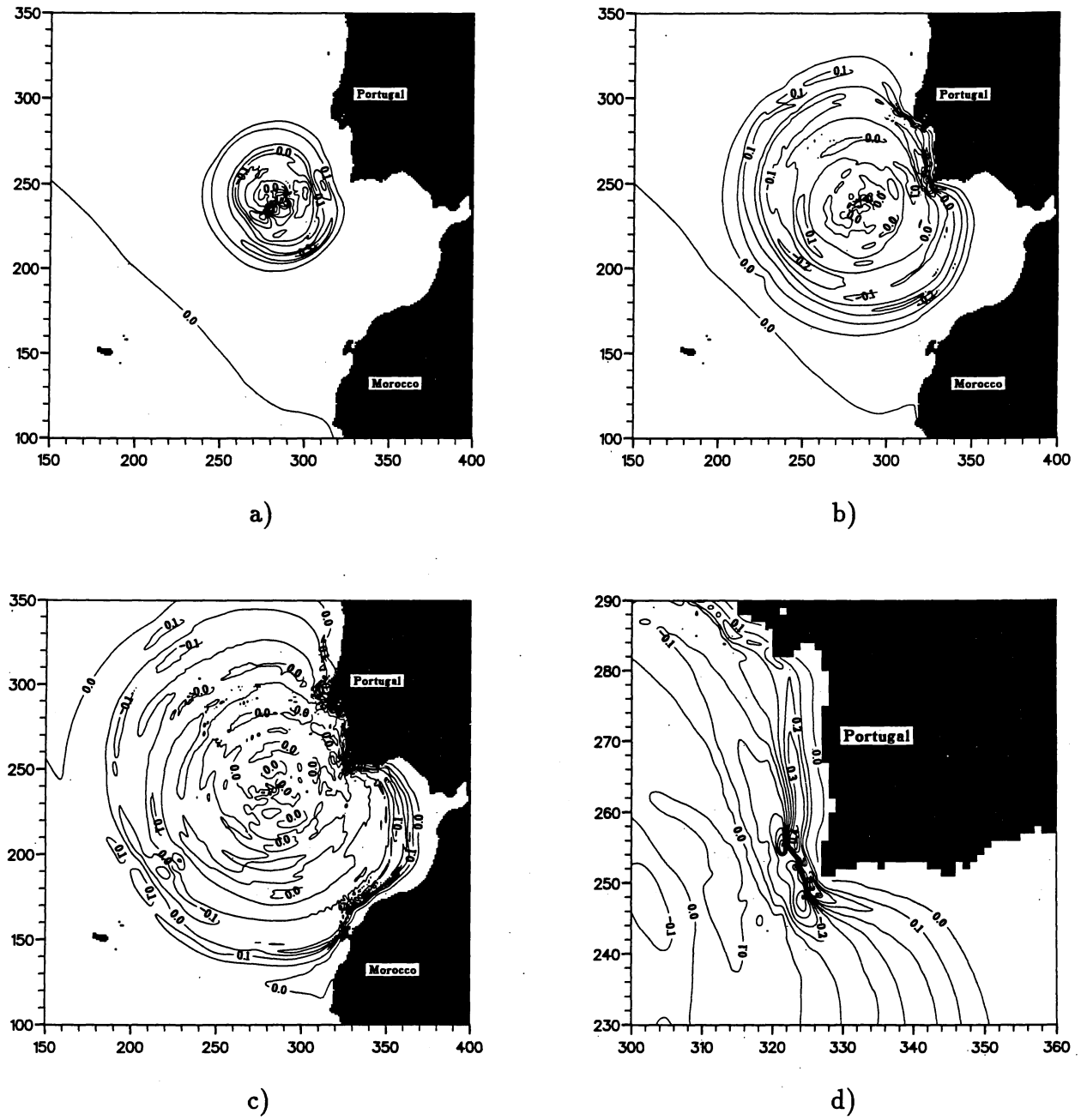

Figure 8: The Gorringe Bank case: Source centered on the bank with $a = 25$ km, $b = 50$ km, $\Delta h = 3$ m. Contour plots of sea surface displacement (m) at time: 0.25 hours (a), 0.50 hours (b), 0.75 hours (c). A blow-up of (b) shown in (d). Grid resolution 5 km. Grid coordinates shown on axis.

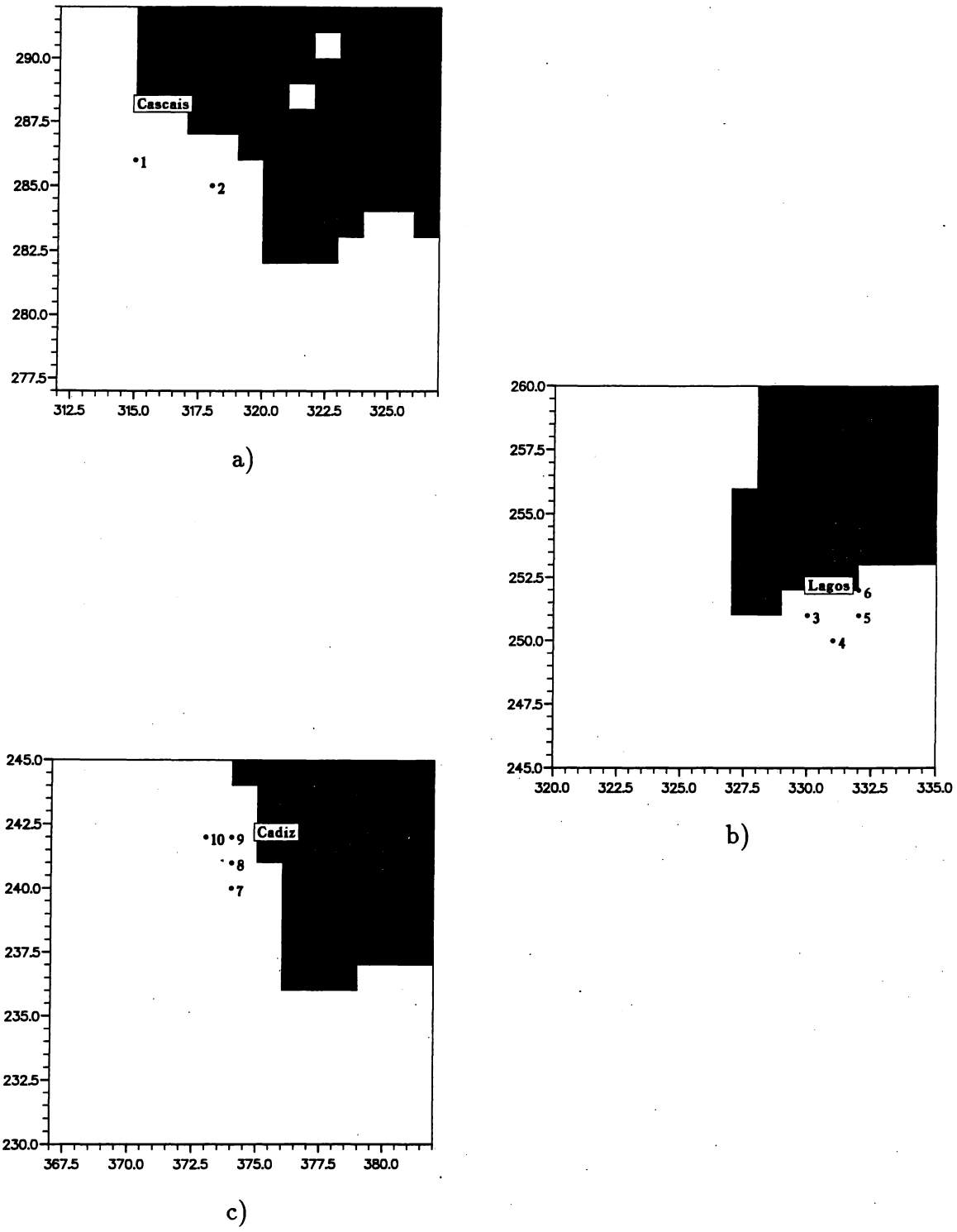

Figure 9: Location of stations off the coasts of Portugal and Spain with modelled time series for sea surface displacement. Grid resolution 5 km. Grid coordinates shown on axis.

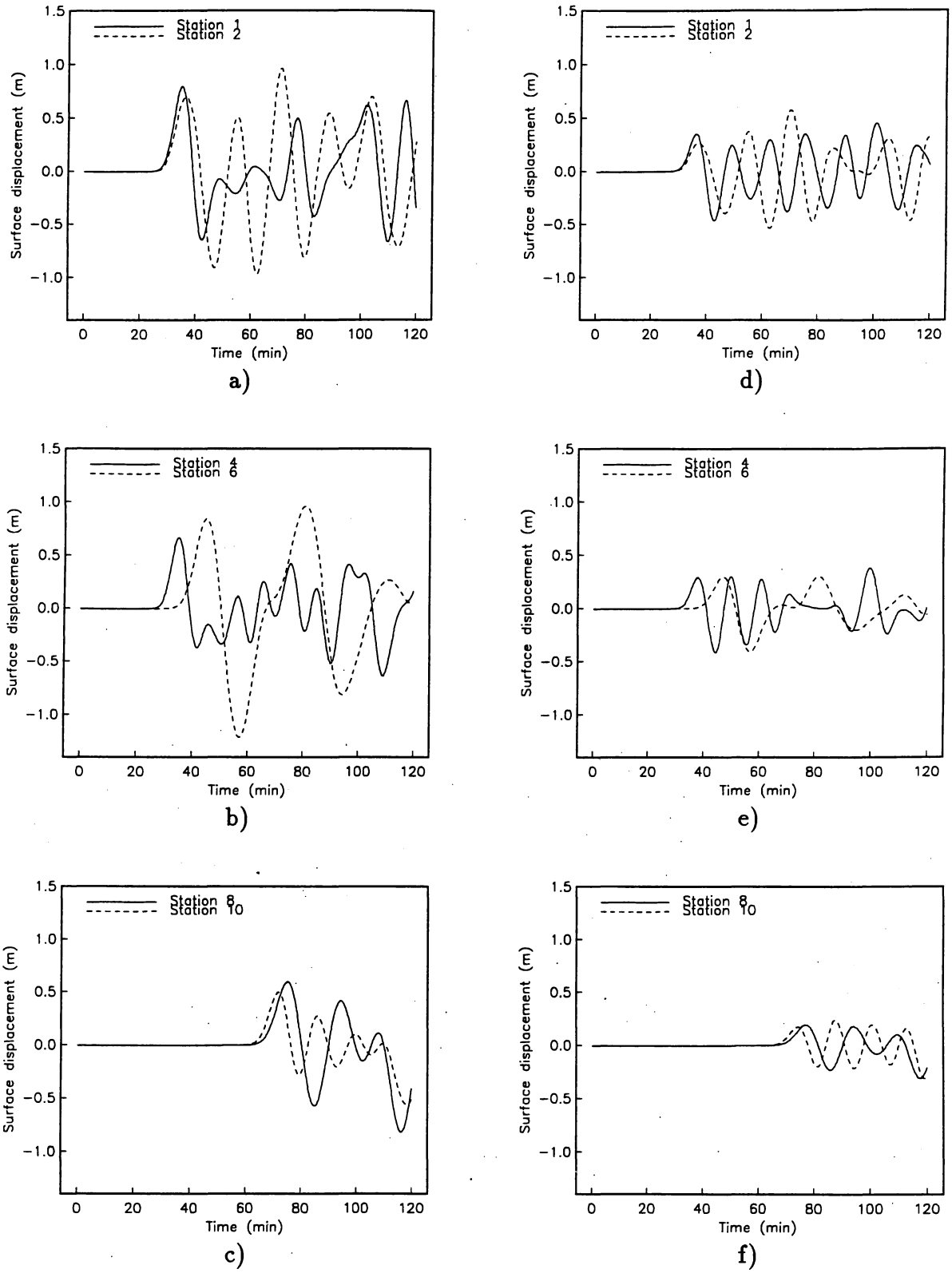

Figure 10: The Gorringe Bank case: Source centered on the bank. Time series for sea surface displacement at station 1,2 near Cascais/Lisbon, station 4,6 near Lagos and station 8,10 near Cadiz. Figure a-c: $a = 50$ km, $b = 100$ km, $\Delta h = 3$ m. Figure d-f: $a = 25$ km, $b = 50$ km, $\Delta h = 3$ m.

with the ridge axis of the Gorringe Bank corresponding to a source angle $\theta = -55°$. The uplift is taken to vary approximately linearly, from Δh at the southern end of the area to zero at the northern end. This is modelled by the asymmetric shape function as described in eq. (25) in the appendix. For comparison a rectangular source area with symmetric shape function corresponding to an uniform vertical displacement has also been used. Simulations both with the source centered; (i) on the Gorringe Bank, (ii) near the epicenter position of the 1969 event south of the bank at (36.09° N, 10.49° W) , and (iii) north of the bank have been performed.

The time scale of the uplift is set less than the time step for the model which is close to 12 seconds, ie. an abrupt start is being assumed, but we have also made one simulation where the uplift occurred over a time span of 2 minutes in order to see the effect of the time duration of the event. The extent of the source area and the amplitude of the displacement are consistent with the estimated seismic moment of $M_o = 6.0 \cdot 10^{20}$ Nm and with $a = 25$ km, $b = 50$ km and $\Delta h = 3$ m leads to an increase in potential energy $E_{pot} = 5.5 \cdot 10^{13}$ Nm for the uplifted area.

For tuning the model better to the observed wave periods we have employed different extents of the source area. In order to retain approximately the same wave amplitude the displacement amplitude has to be modified accordingly.

7.4 Results of simulations with a hydrostatic non-dispersive model

Unless otherwise noted we have used the asymmetric shape function (25) corresponding to a linear variation of the vertical displacement over the source area.

The results of the simulation with the source centered on the Gorringe Bank (grid coordinates 282,240), show a primary wave of elevation propagating away from the source area followed by a downward wave and thereafter by a second wave of elevation (fig. 8a-d). The wave amplitude varies along the circular wave front with high amplitudes particularly in the direction of the coast of Morocco. Effects of wave refraction and amplification due to bottom topography is clearly seen when the waves approach the coast of Portugal particularly near Cabo São Vicente and in the Cascais-Lisbon area (fig.8b,c). Blow-up of fig.8b show details of the wave pattern in the vicinity of the coast of Portugal (fig.8d). In the source area interesting small scale wave patterns, probably due to trapping of wave energy over the Gorringe Bank, can be seen for example in fig.8a,b.

Time series of surface elevation at two stations off the coast of Cascais and Lisbon , four stations off the coast of Lagos and four stations off the coast of Cadiz (fig.9) show considerable variation both in amplitude and phase (fig.10).

Travel time is determined by the first arrival of the wave signal which is defined when surface displacement surpasses a threshold amplitude of 0.05 m. The period of the first wave is estimated to be twice the length of the time interval between the first arrival and the first subsequent zero-crossing of the time series. In order to make comparison with the observed amplitude range (see section 7.1) we have determined the modelled amplitude range for the first wave puls of the simulated timeseries.

With the largest extent of the source area, a = 50 km, b = 100 km, Δh = 3 m, the travel time for the first arrival at the two stations near Cascais ranges from 28.4–28.8 minutes. The corresponding period of the first wave is between 21.4–26.0 minutes and the amplitude range between 1.44–1.60 m. For the stations near Lagos travel time is from 29.0–36.0 minutes with the period of the first wave 19.9–28.9 minutes and amplitude range between 1.0–2.31 m. The large variation in period and amplitude for the latter stations indicate that wave reflection is important. The results are summarized in tables 2–4.

Wave propagation in the shallow coastal zone may increase the travel time considerably, for example will propagation over a grid distance (5 km) in 30 m depth leads to a delay of 4.9 minutes. This may explain why the model travel times for the offshore model stations are shorter than the observed travel time for the coastal station. Since the model stations are located one or two grid distance away from the coast a time interval of 5-10 minutes should be added to the model travel times when comparing with observations (tables 2–4).

Table 2: Comparison with observations; 1969 Event. Stations (1,2) off the coast of Cascais/Lisbon.

Source	Travel time (min)	Period (min)	Amplitude range (m)
On Gorringe Bank a=50 km, b=100 km, Δh=3 m.	28–29	21–26	1.4–1.6
On Gorringe Bank a=25 km, b=50 km, Δh=3 m	31	18–21	0.7–0.8
South of Gorringe Bank a=50 km, b=100 km, Δh=3 m	33	19–22	1.3–1.9
North of Gorringe Bank a=25 km, b=50 km, Δh=3 m.	30	15–20	0.6–0.8
Observations Cascais	37.0	19.2	0.93

In order to tune the model to shorter wave period we have made another experiment with the source centered on Gorringe Bank (grid coordinates 282,240) and with reduced extent of the source area, a = 25 km, b = 50 km, Δh = 3 m. The time series of surface displacement at the same stations as for the previous experiment is shown in fig.10. The period of the first wave is estimated to be 16.1–19.7 minutes for the stations outside Cascais and Lisbon and 14.8–21.8 minutes for the stations off the coast of Lagos. The amplitude

range for the stations near Cascais is 0.67–0.82 m and for stations near Lagos 0.69–0.99 m. These results are in good agreement with the observation (tables 2 and 3). The results from Cadiz (table 4) also fits well with the observations provided the travel time is corrected corresponding to the distance between the off shore stations and the coast.

A simulation has also been done with the source centered south of Gorringe Bank (grid coordinates 300,228), and with a = 50 km, b = 100 km, Δh = 3 m. With this source location, the travel time to Cascais-Lisbon is increased with 3.8–4.4 minutes while the travel time for stations near Lagos is reduced with 7.8–8.2 minutes as compared to the case with the source on the bank (tables 2 and 3).

The simulation with the source north of the Gorringe Bank (grid coordinates 278,244), near the location determined by ray tracing ([2]), lead to too long travel time for stations near Lagos (table 3).

In conclusion this indicates that the 1969 tsunami source was most likely located near the central part of Gorringe bank and not at the estimated epicenter location south of the bank.

Simulations with a symmetric shape function corresponding to uniform distribution of the vertical displacement over the source area shows qualitatively the same results for wave period and travel time, but the directional distribution of the amplitude of the waves may change.

Table 3: Comparison with observations; 1969 Event. Stations (3-6) off the coast of Lagos.

Source	Travel time (min)	Period (min)	Amplitude range (m)
On Gorringe Bank a=50 km, b=100 km, Δh=3 m.	29–36	20–29	1.0–2.3
On Gorringe Bank a=25 km, b=50 km, Δh=3 m.	34–41	15–22	0.7–1.0
South of Gorringe Bank a=50 km, b=100 km, Δh=3 m.	21–28	19–30	1.3-2.2
North of Gorringe Bank a=50 km, b=100 km, Δh=3 m.	36–44	13–21	0.5-0.7
Observations Lagos	35.5	14.4	0.84

Table 4: Comparison with observations; 1969 Event. Station (7-10) off the coast of Cadiz.

Source	Travel time (min)	Period (min)	Amplitude range (m)
On Gorringe Bank a=50 km, b=100 km, Δh=3 m.	65–69	23–30	0.8–1.4
On Gorringe Bank a=25 km, b=50 km, Δh=3 m	69–74	17–22	0.4–0.5
South of Gorringe Bank a=50 km, b=100 km, Δh=3 m	56–60	23–30	1.0–1.5
North of Gorringe Bank a=25 km, b=50 km, Δh=3 m.	73–77	15–21	0.3
Observations Cadiz	84	16	0.38

It remains to investigate the effect of an area with downward displacement of the seabed on the southern side of the fault. This will mainly effect the primary wave on The Canary Islands and Madeira, and along the coast of Morocco. The sea level observations from The Canary Islands and Madeira for the 1969 event are of poor quality and cannot be used to confirm the existence of a downward motion of the first wave. Unfortunately observations from the coast of Morocco, which would have been crucial for determining the distribution of a possible subsidence zone in the source area, have been impossible to obtain. Unconfirmed records of a 1.2 m tsunami wave at Casablanca during the 1969 event fits well with the results of the simulations reported above.

7.5 Results of simulation with a nonlinear dispersive model

The bathymetry at the Gorringe ridge strongly suggest that nonlinear effects may be important for large vertical displacements of the sea bed (Δh). To estimate nonlinear and dispersive effects we have compared the predictions from four different approximations to the Boussinesq equations:

(i) All higher order terms in α and ϵ are omitted: linear hydrostatic equations – labelled 'lin. hyd." in fig. 11 and 12.

(ii) All higher order terms in ϵ are omitted: nonlinear hydrostatic equations (Airys equations) – labelled 'non-lin.' in the figures.

(iii) The higher order terms in ϵ are kept, whereas all nonlinearity is deleted: linear dispersive equations – labelled 'disp.' in the figures.

(iv) The full Boussinesq equations – labelled 'Bouss.' in the figures.

The nonlinear and dispersive computations are performed for a 450 km $\times$ 400 km domain ranging from gridpoint (230,200) to (320,280) of the standard depth matrix. Within this subdomain the depth data are interpolated and smoothened to enable numerical integration with grid increments 1.25 km and 2.5 km in addition the standard increment of 5 km. Due to the coarseness of the initial data, the stereographic transformation and the smoothing the minimum depth at the Gorringe bank has been increased to ap. 280 m as opposed to the correct value of 25 m at the summit of the Gettysburg seamount. To bring the representation of bank closer to reality we have subtracted a symmetric function of type (25) from the depth in the proximity of the ridge, resulting in a minimum depth of 50 m for the finest grid. The topography in the vicinity of the Gorringe ridge is depicted in fig. 11a together with the locations of the time serie stations A-I and the extension of the source area.

In all the simulations reported in the present subsection we have replaced the fault by an initial surface elevation as described at the end of section 4. The source is localized at the Gorringe ridge, is shaped according to the symmetric function (25) and has horizontal extensions as given in sec. 7.3 (a = 50 km, b = 100 km, $\theta = -55°$). We employ three different displacement amplitudes: Δh = 3m, 7m, 15m.

Some results from the simulations are selected for presentation in figure 11b through 12c. At location A (11b) the dispersive effects modify the leading pulse and generates trailing oscillations while nonlinear effects are absent. At G all approximations yield very close results. These results are typical for all stations in the far field range and all values of Δh. They indicate that dispersive effects are more important for wave-propagation in the direction across than in the direction along the Gorringe bank. The most obvious reason is that the length scales are larger in the lateral direction for both bathymetry and source. Even for the largest Δh the nonlinearities become significant only at the most shallow stations, namely C and F close to the peaks of the Gettysburg and Ormonde seamounts respectively. The depth at station C is 52.5 m and the most striking feature of the time series (fig. 11d, 12b) is the large depression after approximately 10 min. For the largest Δh (15 m) we obtain a minimum η of ca. -60 m which indicate that the peak of the Gorringe ridge in fact becomes dry. Still the nonlinear effects primarily delay the occurrence of the minimum for η whereas linear theory gives an overall correct picture until t =12 min, say. However, according to the discussion below the validity of the time series at C is questionable.

The effect of discretization errors at A is demonstrated in fig. 12a. Clearly the standard resolution Δx = 5 km yields an appreciable artificial dispersion, whereas the results for the two finer grids are very close. Still comparing with the results of the Boussinesq equations in fig. 11b, the coarse grid do in fact produce the best solution. The explanation

is quite simple. Fulfillment of the Courant criterion (7) implies a numerical dispersion of the normal type. Provided the numerical dispersion is less or comparable to the real dispersion its presence will thus generally improve the results. However, at station C (Gettysburg) we do not observe any sign of convergence for decreasing Δx even for $\Delta h = 3$ m (fig. 12b). On the contrary, the behaviour becomes increasingly irregular with grid refinement. This is confirmed by the cross sectional graphs depicted in fig. 12c. The results for Δx=1.25 km were in fact to messy to be included in the figure. We are led to conclude that even the resolution Δx=1.25 km is far to crude near the peaks of the Gorringe bank. To investigate the numerical problems further we have performed two dimensional simulations with bathymetry and source corresponding to a North-South cross-section through C (see figure 12c). For Δx=5, 2.5 and 1.25 km we observed similar grid dependence as in figure 12b. When the grid increments were reduced this feature vanished and the solution had converged properly for $\Delta x \sim 100$ m, say. We note that a corresponding resolution of the 450 km $\times$ 400 km domain round the Gorringe Bank requires 20 mill. gridpoints, whereas a refinement of the total depth matrix would amount to 300 mill. points. The problem can be circumvented in three different ways: applying a curvilinear grid, nesting of a refined grid at the bank to a coarser grid for the far-field or using a finite element discretization. In two dimensions we have produced very accurate solutions using a nonuniform grid with a small total number of points. Unfortunately, nonuniform grids cannot be employed equally simple and effectively in the three-dimensional case.

There was a striking difference in the minimum value of η at C as obtained by the three and two dimensional simulations. For $\Delta h = 7$m the two dimensional calculations gave approximately 12 m as compared to 30 m in figure 11d. This suggest that the pronounced depression after about 10 min mainly is a three dimensional effect related to the very shallow peak of the Gettysburg seamount. The results at E and F confirm this assumption. For large Δh, especially if combined with the true minimum depth of 25 m, we may possibly even encounter wave breaking. Such features will be further analyzed in subsequent work and we plan employ the finite element method for the Boussinesq equation and investigate the possibility of breaking by means of a boundary integral technique for 2-D Laplace equation with a fully nonlinear free surface boundary condition .

A complete set of simulations have also been performed without the depth corrections mentioned above. In these calculations there is no sign of irregular behaviour at the ridge, indicating that such effects occur in very shallow water only. In fig. 12d we have compared time series at A obtained from the corrected (depth 50 m) and the uncorrected (standard) depth matrices respectively. While the leading pulses are virtually equal the corrected depth matrix displays lower amplitudes and a time delay for the proceeding waves. This is as can be expected from Greens law [9] and the dispersion relation for linear waves on constant depth.

We may conclude that the nonlinearity do not affect the motion in the far field, even though it will be of some importance at the peaks of the Gorringe ridge. This is probably due to the fact that the shallow regions are to narrow to allow the nonlinear effects sufficient time to heavily influence the leading pulse. Dispersive effects are however significant, but by no means crucial, for the far field motion. For the standard grid the discretization errors in the far field are of the same order of magnitude as the dispersive effects, which

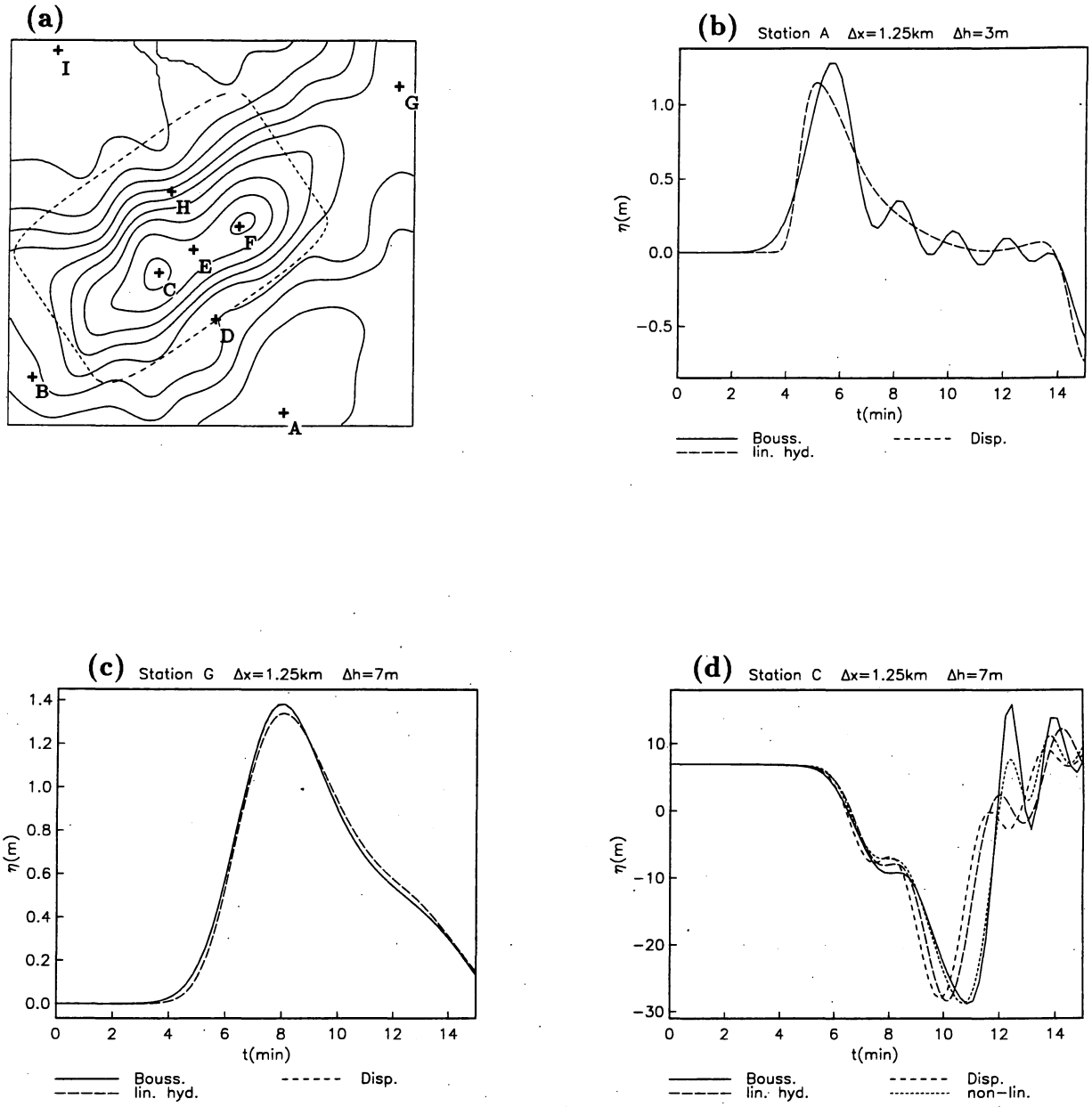

Figure 11: Local analysis on the Gorringe bank. (a): Bathymetry and location of the stations. Displayed region: 175km×162.5km, depth contours: h = 200m,800m,1400m,.... The dashed line displays the $0.1\Delta h$ contour of the initial disturbance. (b,c,d): Time series for the surface elevation, η.

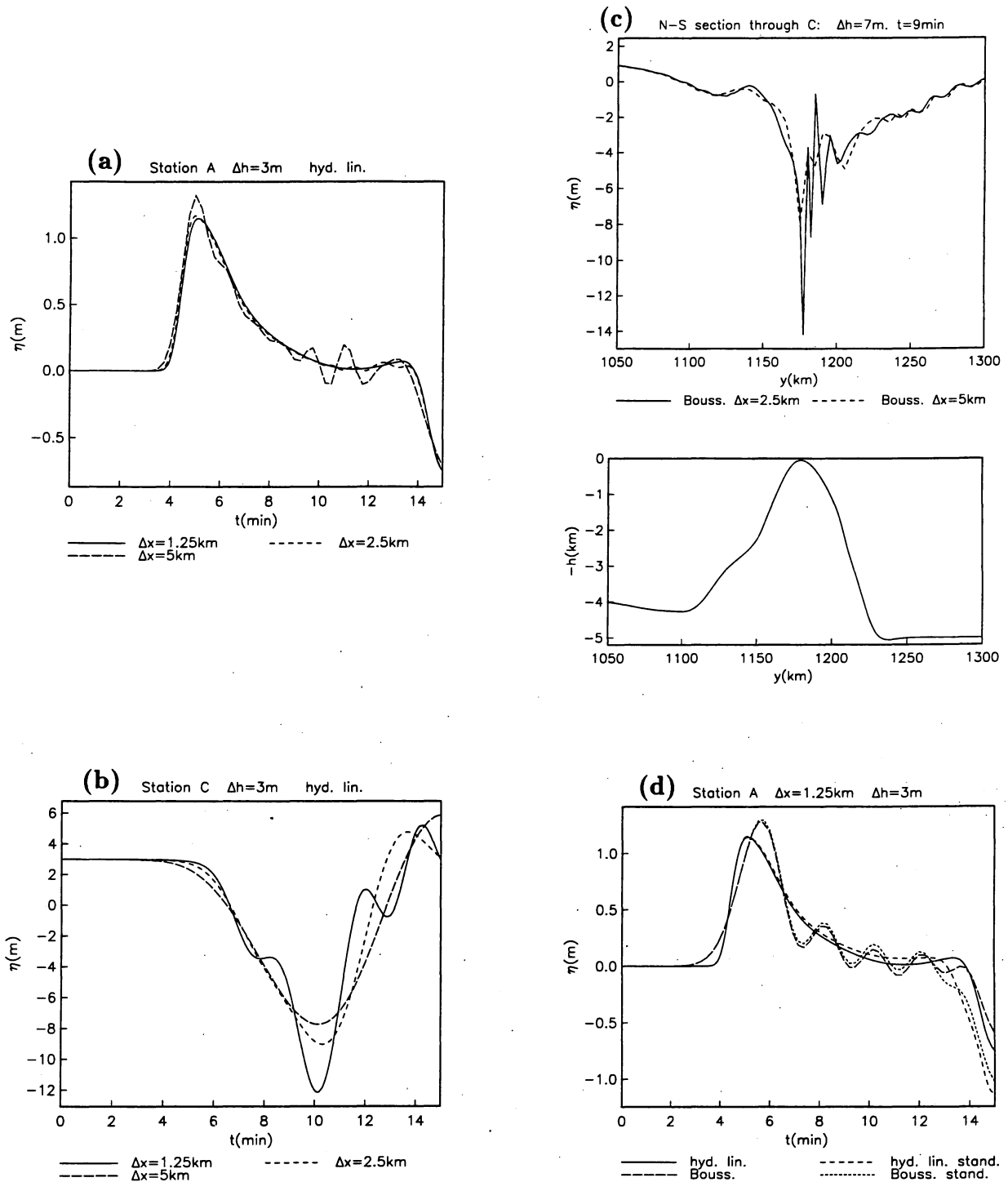

Figure 12: Local analysis on the Gorringe bank. (a,b): Time series with grid refinement. (c): North-South cross-section through station C, upper panel: η, lower panel: h. (d) Comparison to results from the directly interpolated standard depth matrix (stand.).

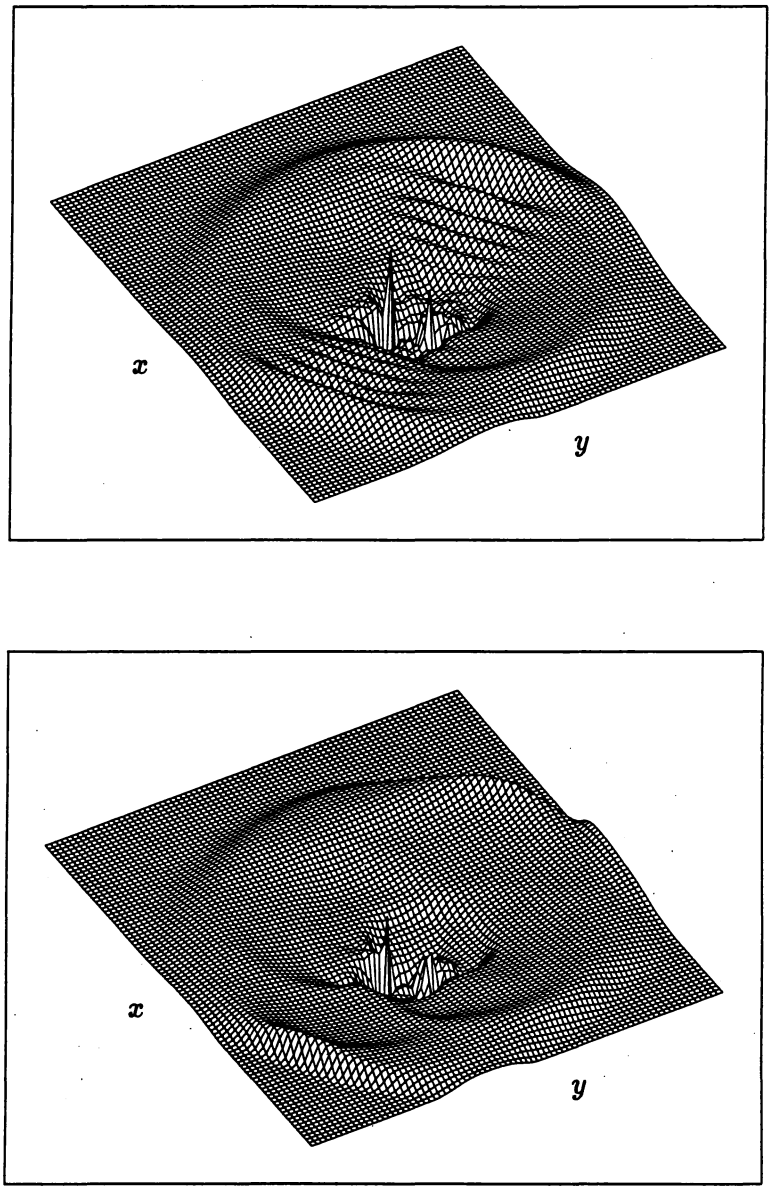

Figure 13: Surface displacement over the Gorringe bank at $t = 12$ min. for Δh=3 m, viewed from South-East. The gridsize is 1.25×1.25km with every fourth grid-lines depicted. Upper panel: Boussinesq solution, lower panel: linear hydrostatic solution.

in fact suggest that the grid size of 5 km is most appropriate for integration of the linear hydrostatic equations. At the Gorringe ridge, on the other hand, the grid is far to coarse to reproduce local effects properly. It must be anticipated that grid refinement may be highly desirable also in the coastal regions, where the above type of local analysis is far more important than at the Gorringe bank. However, such work would require access to more accurate bathymetric data than those available to us at present.

8 The Thera case study

8.1 Observational evidence

The Aegean Sea and the Greek Archipelago have been the center of many large tsunami events as shown by the catalogue compiled by Papadopoulos et.al. [11]. Among the most famous events is the Minoan eruption of the Santorini (Thera) volcano about 1400 B.C. where waves generated by the caldera formation have been believed to wipe out many towns and harbours in Crete. Although there is no recorded data from this event we have attempted to model wave propagation from a collapsing Santorini volcano. The results serve to demonstrate typical features of tsunami wave propagation in these waters and must be regarded as a preliminary exercise for modelling more well-documented events as for example the 9 July 1956 event with source at the Amorgos Island [1], [12].

8.2 The depth matrix

By using the world topographic matrix ETOPO we have compiled a depth matrix with a stereographic map projection for the eastern Mediterranean including the Aegean Sea and the Greek Archipelagos. The center of the pole of the projection is chosen at 36° N and 26° W, with a grid resolution of 5 km × 5 km (fig. 14) . Due to the rather coarse resolution of the ETOPO (5 × 5 minutes) and its inherent deficiencies the resulting interpolated depth matrix is not very accurate. Before further attempts to model tsunami propagation in the Greek Archipelagos is undertaken with islands and small scale variation in bottom topography, a more accurate depth matrix with finer resolution should be established.

8.3 The models of the tsunami source

As a crude model of the collapsing volcano we have adapted a downward sinking of the sea bed in form of a Gaussian bell with maximum downward displacement $\Delta h = 100$ m and with two different values of the radius: $a = b = 10$ km. In the model the displacement is set to occur instantaneously corresponding to starting with a surface displacement of same form as the displacement of the sea bed.

8.4 Results of simulations

Contour plots of the sea surface show a front wave with downward surface displacement propagating away from Santorini in a circular pattern followed by a wave with upward

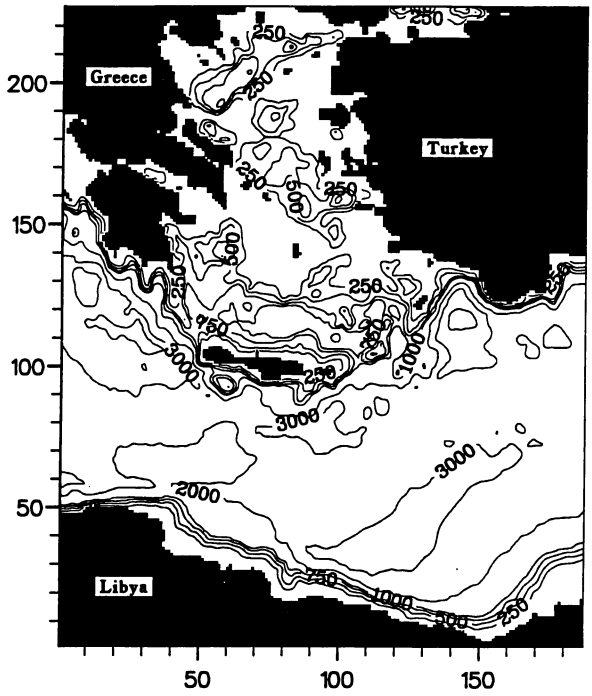

Figure 14: Model domain for eastern Mediterranean and the Greek Archipelago. Depth contours in meters. Stereographic map projection with pole at 36° N, 26° W. Grid resolution 5 km. Grid coordinates shown on axis.

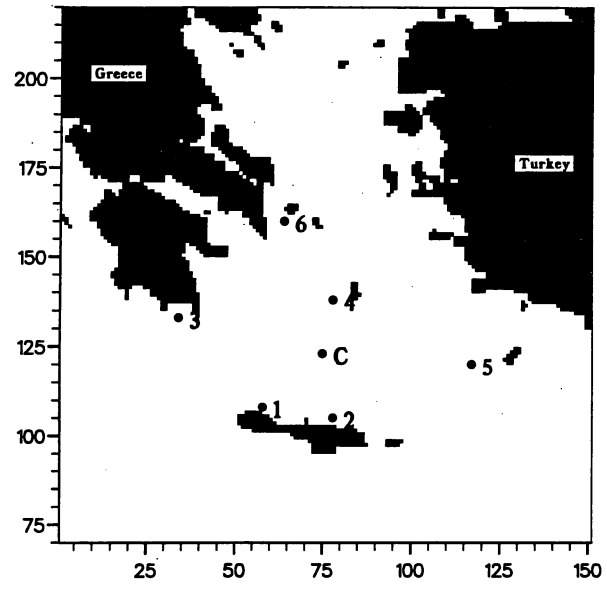

Figure 15: Location of stations with modelled time series for sea surface displacement. The center of the source is marked C.

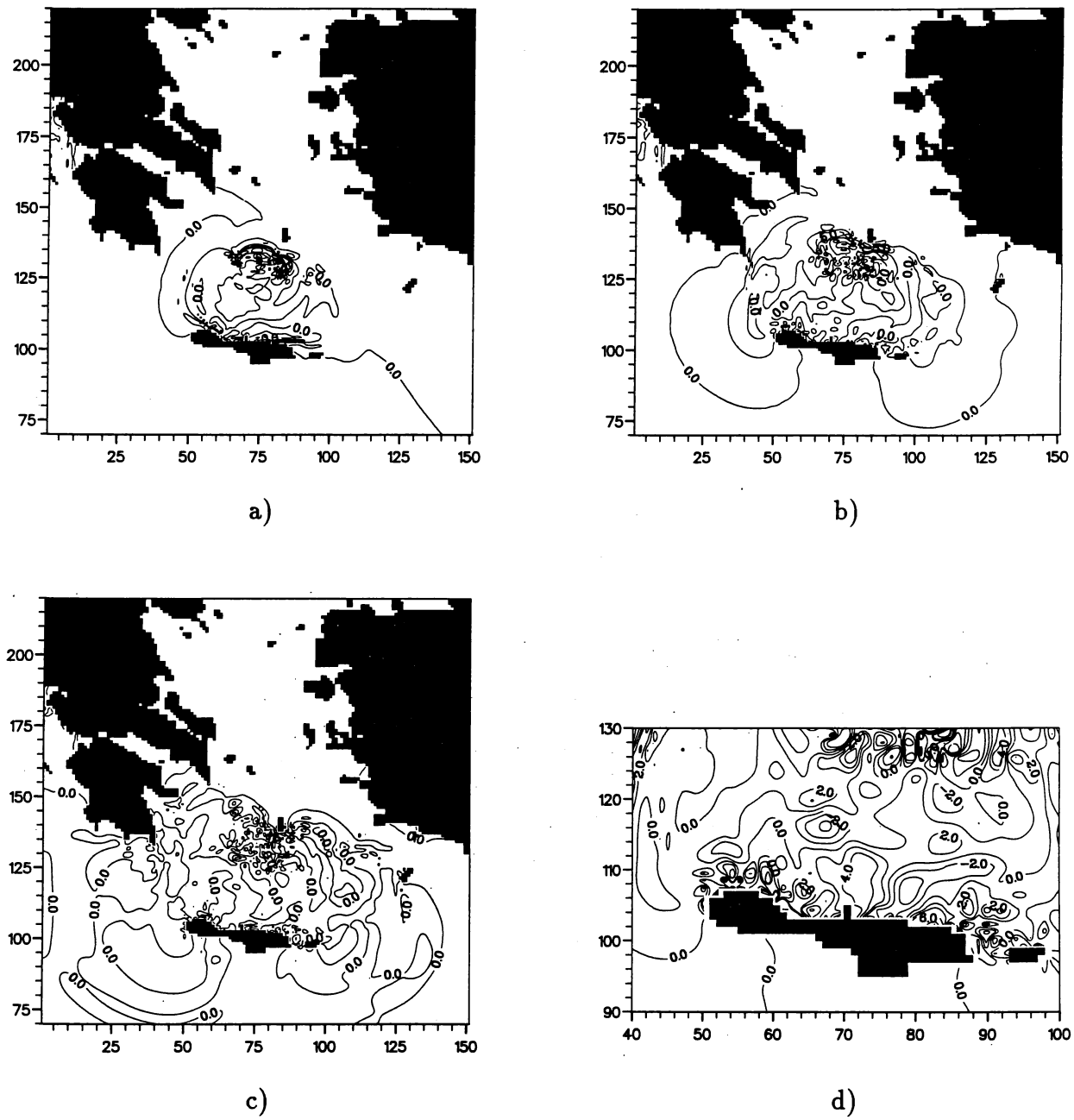

Figure 16: The Thera case: Contour plots of sea surface displacement (m) for time: 0.50 hours (a), 0.72 hours (b) and 1.01 hours (c) after instantaneous start. A blow-up of (b) is shown in (d). Radius of source $a = b = 10.0$ km. Grid resolution: 5.0 km.

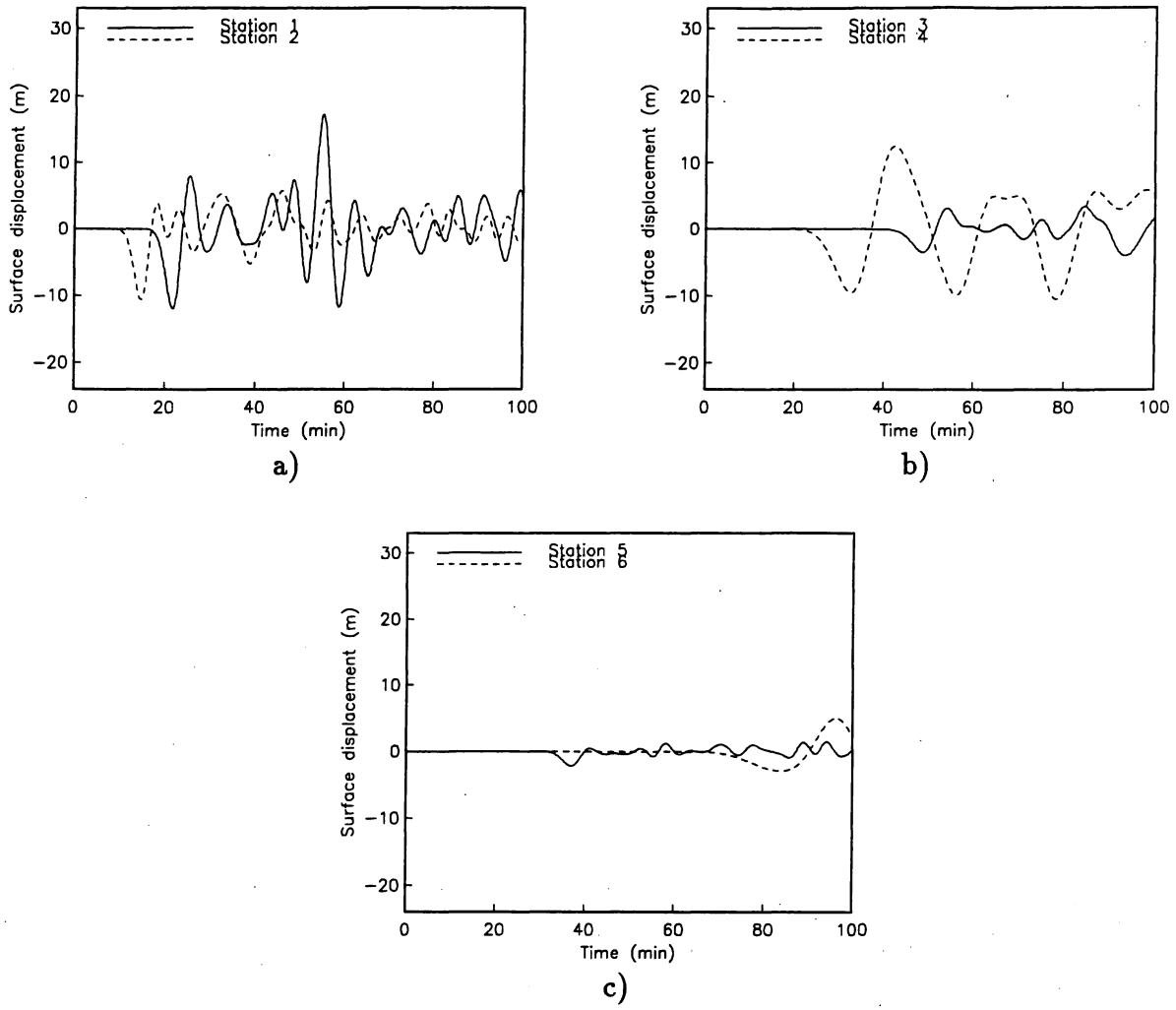

Figure 17: The Thera case: Time series for sea surface displacement at station 1 - 6. Radius of source $a = b = 10.0$ km. Grid resolution: 5.0 km.

surface displacement (fig. 16). As time goes the tail of the wave pattern breaks up in many small scale wavelets probably due to reflection . Strong reflection pattern are clearly visible along the northern coast of Crete where time series from stations 1 and 2 (fig. 17**a**) show wave amplitudes up to 18 m above mean water level. A striking feature of these time series is the occurrence of several oscillation with period about 12 minutes particularly at a station on the northwestern coast of Crete. The open oceanic gap between the western end of Crete and the Greek mainland is seen to generate a diffracted wave pattern (fig 16). Time series from stations off the coast of the Greek mainland, stations 3 and 6, (fig. 17b,c) show lower wave amplitudes than along the coast of Crete. In view of the rather crude grid resolution we must expect the reported results to be somewhat hampered by discretization errors. We plan to perform computations on a substantially refined grid in the near future.

9 Concluding remarks.

The preliminary results of case studies reported above demonstrate the status of our model development and the capability to simulate real events. The results obtained for the 1969 event at the Gorringe Bank are particularly promising. In this case were the calculated tsunami wave amplitude and period can be compared with observational data we find good agreement. It is also interesting to note that the source parameters used for these simulations are consistent with the geological constraints and observed seismic moment for the event. The few sensitivity tests we have done show that better agreement can be expected by optimal tuning of the source parameters.

The effects of non-linearity and dispersion are studied solving the Boussinesq equations in the near source region. Non-linear effects are important on the shallow parts of the Gorringe Bank, where wave breaking may take place even for a small amplitude event as in 1969. The primary wave puls in the far-field region is however well described with a linear model.

A more accurate depth matrix with finer resolution particularly near the source and in runup zones near the coast may also be important for improving the performance of the model. Access to all available recorded data of wave amplitude and period along the coast of Portugal and Morocco and from island stations on Canary Island and Madeira is important for the progress of the validation of the model predictions. Unfortunately the data for the 1969 event from Canary Island and Madeira are of poor quality and cannot be used to confirm the existence of an area of downward vertical displacement of the seabed on the southern side of the fault. Data from the coast of Morocco, which also could have provided a clue to this problem, has been impossible to obtain.

The results of the Thera case study are more loosely rooted, and we miss the guidance from data records and seismic or geological constrains on the source parameters. Further simulations of this test case may await new geological evidence of tsunami runup. With a more accurate depth matrix with finer grid resolution than the one available at the moment it would be interesting to simulate a more well documented case, for example the 1956 Amorgos Island event.

Acknowledgment

The participation of the Oslo group in the GITEC project has been funded by the Norwegian Research Council (NTNF). We are indebted to Mr. Per Moen, University of Oslo, for help with the derivation of formulas for the transformation to stereographic map coordinates.

Appendix

A Source shapes

A Gaussian bell form function is defined by;

$$S(q_1, q_2) = \exp\left[-(q_1)^2 - (q_2)^2\right] \tag{24}$$

Another function, closer to a square in shape, is defined by;

$$S(q_1, q_2) = \exp\left[-(2q_2)^4\right] f(q_1) F(q_1) \tag{25}$$

where

$$F(q_1) = \begin{cases} 1 & \text{if } |q_1| < \frac{1}{2} \\ \exp\left[-4\left(|q_1| - \frac{1}{2}\right)^4\right] & \text{if } |q_1| > \frac{1}{2} \end{cases} \tag{26}$$

and a symmetric and an asymmetric source is obtained by choosing $f(q_1) = 1$ and $f(q_1) = 1 + \frac{3}{2}q_1$ respectively.

References

[1] Ambraseys, N. N., (1960) The Seismic Sea Wave of July 9, 1956, in the Greek Archipelago *J. Geophys. Res.* , Vol. **65**, No **4** 1257–1265.

[2] Baptista, Maria Ana, Miranda, Pedro, and Mendes Victor, Louis, (1992) Maximum Entropy Analysis of Portuguese Tsunami Data. The tsunamis of 28.02.1969 and 26.05.1975. *Int. J. of The Tsunami Soc.* Vol. **10** No. **1** ,p 9-20.

[3] Bondevik, S. and Svendsen J. I., (1993) Paleotsunamis in the Norwegian Sea and the North Sea. *GITEC, Annual report, University of Bergen, Oct. 1993.*

[4] Fukao Yoshio, (1973) Thrust faulting at a lithospheric plate: Boundary the Portugal earthquake of 1969. *Earth and Planetary Sci. Let. Vol. 18, 205–216*

[5] Gjevik, B., Høvik, O. og Moe, H. (1992) Simuleringer av tidevannet i kystområdet innenfor Haltenbanken. *Rapport TJ-92-1 to STATOIL*, Dept of Math.,University of Oslo. (In Norwegian)

[6] Gjevik, B., and Straume, T., (1989) Simulations of the M_2 and the K_1 tide in the Nordic Seas and the Arctic Ocean. *Tellus* **41A**, 73-96.

[7] Harbitz C. B. (1992) Model simulations of tsunamis generated by the Storegga Slides. *Marine Geology*, Vol. **105**, 1-21.

[8] Harbitz, C. B., Pedersen, G., and Gjevik, B., (1993) Numerical simulation of large water waves due to landslides. *J. Hydraulic Enginering.* In press.

[9] Mei, C. C., (1989) The applied dynamics of ocean surface waves. *Advanced Series on Ocean Engineering* Vol.**I**, 740 pp. World Scientific, London.

[10] Mesinger, F., and Arakawa, A., (1976) Numerical methods used in atmospheric models. *GARP Publ. Ser*, **17**, 64 pp. World Meterological Organization.

[11] Papadopoulos, G.A., and Chalkis, B. J. (1984) Tsunamis observed in Greece and the surrounding area from antiquity up to the present times *Marine Geology*, Letter sec. Vol. **56**, 309–317.

[12] Papadopoulos, G.A., and Pavlides, S. B. (1992) The large 1956 earthquake in the South Aegean: Macroseismic field configuration, faulting, and neotectonics of Amorgos Island. *Earth and Planetary Science Letters*, **113** 383–396.

[13] Pedersen, G., Rygg, O.B. (1987) Numerical solution of the three dimensional Boussinesq equations for dispersive surface waves. *Research Report in Mechanics*, **88–1**, University of Oslo.

[14] Pedersen G. (1988) Three-dimensional wave patterns generated by moving disturbances at transcritical speeds. *J. Fluid. Mech.* Vol. **196**, 39-63.

[15] Pedersen G. (1988) On the numerical solution of the Boussinesq equations. *Research Report in Mechanics*, **88–14**, University of Oslo.

[16] Pedersen G. (1991) Finite difference representations of nonlinear waves. *Int. Journal Num. Meth. in Fluids* **13**, 671-690.

[17] Ribeiro Antonio (1982) Tectónica de Placas: Aplicação à sismotecttónica e à evolução da fronteira de placas Açores–Gibraltar. *Geonovas, Revisita da Associacao Portuguesa de Geologos, No 4, 87–96*

[18] Wu T.Y. 1981 Long waves in ocean and coastal waters. *Proc. ASCE, J. Eng. Mech. Div.* **107**,EM3, 501–522.